TU Delft

Delft University of Technology

Cleavage fracture micromechanisms in simulated heat affected zones of S690 high strength steels

Bertolo, V.; Jiang, Q.; Terol Sanchez, M.; Riemslag, T.; Walters, C. L.; Sietsma, J.; Popovich, V.

DOI
10.1016/j.msea.2023.144762

Publication date
2023

Document Version
Final published version

Published in
Materials Science and Engineering A

Citation (APA)
Bertolo, V., Jiang, Q., Terol Sanchez, M., Riemslag, T., Walters, C. L., Sietsma, J., & Popovich, V. (2023). Cleavage fracture micromechanisms in simulated heat affected zones of S690 high strength steels. *Materials Science and Engineering A*, *868*, Article 144762. https://doi.org/10.1016/j.msea.2023.144762

Important note
To cite this publication, please use the final published version (if applicable).
Please check the document version above.

Copyright
Other than for strictly personal use, it is not permitted to download, forward or distribute the text or part of it, without the consent of the author(s) and/or copyright holder(s), unless the work is under an open content license such as Creative Commons.

Takedown policy
Please contact us and provide details if you believe this document breaches copyrights.
We will remove access to the work immediately and investigate your claim.

This work is downloaded from Delft University of Technology.
For technical reasons the number of authors shown on this cover page is limited to a maximum of 10.

Materials Science & Engineering A 868 (2023) 144762

Contents lists available at ScienceDirect

Materials Science & Engineering A

journal homepage: www.elsevier.com/locate/msea

Cleavage fracture micromechanisms in simulated heat affected zones of S690 high strength steels

V. Bertolo [a,*], Q. Jiang [a], M. Terol Sanchez [a], T. Riemslag [a], C.L. Walters [b,c], J. Sietsma [a], V. Popovich [a]

[a] Materials Science and Engineering, Delft University of Technology, Mekelweg 2, 2628 CD, Delft, the Netherlands
[b] Structural Dynamics, TNO, Molengraaffsingel 8, 2629 JD, Delft, the Netherlands
[c] Maritime and Transport Technology, Delft University of Technology, Mekelweg 2, 2628 CD, Delft, the Netherlands

ARTICLE INFO

Keywords:
High strength steel
Gleeble
HAZ
Cleavage fracture toughness
M-A constituents
Pop-in

ABSTRACT

High strength steels are widely used for structural applications, where a combination of excellent strength and ductile-to-brittle transition (DBT) properties are required. However, such a combination of high strength and toughness can be deteriorated in the heat affected zone (HAZ) after welding. This work aims to develop a relationship between microstructure and cleavage fracture in the most brittle areas of welded S690 high strength structures: coarse-grained and intercritically reheated coarse-grained HAZ (CGHAZ and ICCGHAZ). Gleeble thermal simulations were performed to generate three microstructures: CGHAZ and ICCGHAZ at 750 and 800 °C intercritical peak temperatures. Their microstructures were characterised, and the tensile and fracture properties were investigated at − 40 °C, where cleavage is dominant. Results show that despite the larger area fraction of martensite-austenite (M-A) constituents in ICCGHAZ 750 °C, the CGHAZ is the zone with the lowest fracture toughness. Although M-A constituents are responsible for triggering fracture, their small size (less than 1 μm) results in local stress that is insufficient for fracture. Crack propagation is found to be the crucial fracture step. Consequently, the harder auto-tempered matrix of CGHAZ leads to the lowest fracture toughness. The main crack propagates transgranularly, along {100} and {110} planes, and neither the necklace structure at prior austenite grain boundaries of ICCGHAZs nor M-A constituents are observed as preferential sites for crack growth. The fracture profile shows that prior austenite grain boundaries and other high-angle grain boundaries (e.g., packet and block) with different neighbouring Bain axes can effectively divert the cleavage crack. Moreover, M − A constituents with internal sub-structures, which have high kernel average misorientation and high-angle boundaries, are observed to deflect and arrest the secondary cracks. As a result, multiple pop-ins in load-displacement curves during bending tests are observed for the investigated HAZs.

1. Introduction

The balance between high strength and high fracture toughness required for structural applications, such as for components in heavy lifting equipment and wind farms, is found in high strength steels even at such low temperatures as − 60 °C (e.g., in the Arctic). However, this balance usually is compromised by welding processes used for connecting structural components. The welding thermal input modifies the base material microstructure and generates heat-affected zones (HAZ) with complex microstructures and potentially poor toughness. For single- and multi-pass welding – needed for thick-section steel plates –, the coarse-grained heat affected zone (CGHAZ) and the intercritically reheated coarse-grained heat affected zone (ICCGHAZ) are the areas with the lowest toughness as a consequence of preferential failure sites. Due to the formation of brittle zones, the ductile-to-brittle transition temperature of high strength steels is shifted as a result of welding from around − 80 °C to approximately − 30 °C, raising concern in terms of cleavage fracture [1].

Many authors [2–5] have reported that the degradation of fracture properties of CGHAZ and ICCGHAZ are related to the coarsening of austenite grains and the formation of martensite-austenite (M-A) constituents. Extensive investigation on the effect of different M-A parameters, such as size, volume fraction and morphology, on toughness, has also been carried out [6–10]. It is well established that the larger the size

* Corresponding author.
E-mail address: v.moretebarbosabertolo@tudelft.nl (V. Bertolo).

https://doi.org/10.1016/j.msea.2023.144762
Received 15 November 2022; Received in revised form 26 January 2023; Accepted 8 February 2023
Available online 10 February 2023
0921-5093/© 2023 The Authors. Published by Elsevier B.V. This is an open access article under the CC BY-NC-ND license (http://creativecommons.org/licenses/by-nc-nd/4.0/).

and volume fraction of M-A constituents, the lower the fracture toughness [6–8]. On the other hand, there is no consensus on the morphological effect of M-A constituents on toughness. The two most detrimental M-A morphologies are blocky (or massive) and slender (or elongated). While Bayraktar and Kaplan [6], Kumar and Nath [7], and Li and Baker [10] observed that the blocky M-A constituents are more detrimental than the slender ones, Kim et al. [8] and Luo et al. [9] have found that the slender M-A has a more negative impact than the blocky ones. Hence, the knowledge available in the literature regarding the morphological effect of M-A constituents on fracture toughness does not allow us to understand the cleavage behaviour and micromechanisms in CGHAZ and ICCGHAZ in high strength steels.

Furthermore, the effects of the microstructural features of the base material on the fracture toughness of HAZ are barely discussed in the literature. Although the discussions involving the degradation of the mechanical and fracture properties of HAZ are mostly related to M-A constituents, microstructural features in HAZ inherited from the base material, such as brittle inclusions, may also play a role. In previous work by the present authors [11], Nb-rich inclusions were recognised as the most deleterious microstructural feature of a base S690QL high strength steel. In general, Nb-rich inclusions have higher nanohardness than M-A constituents (in the range of 20–25 GPa and 4–11 GPa, respectively), which causes them to be more prone to fracture than M-A constituents [12–14]. Nevertheless, parameters such as size, area fraction and spatial distribution can also influence the criticality of the brittle particles, and it is currently unknown which of these features act as the weakest microstructural sites. Some authors [10,15] analysed steels containing pre-existing carbides and brittle inclusions in the base material that could trigger the fracture process in HAZ. Li and Baker [10] analysed a V and Nb microalloyed steel in which, compared to M-A constituents, pre-existing carbides and aluminium oxide inclusions did not have a significant impact on the toughness of ICCGHAZ. In this case, the carbides were present as thin particles and one order of magnitude smaller than M-A constituents, behaving as isolated particles and not having a major effect on toughness, while the number density of inclusions was quantified as significantly lower than the M-A density. In contrast, pre-existing TiN inclusions in an ultra-low carbon bainitic steel studied by Vassilaros [15] were observed to trigger cleavage fracture in the thermally simulated CGHAZ instead of M-A constituents. It is thus clear that no clear trend has been identified on the cleavage initiation micromechanism in welded steels with different types of brittle particles. Therefore, it needs to be further analysed in order to fully understand the cleavage micromechanisms involved in a multi-phase steel such as S690 high strength steel.

In the present study, thermal welding simulations via Gleeble were carried out to create large sections of CGHAZ and of ICCGHAZ with peak temperatures of 750 °C and 800 °C. The simulated microstructures were analysed and quantified using different techniques that include local chemical composition analysis, microscopy and hardness. The cleavage fracture toughness of the generated CGHAZ and ICCGHAZs was obtained through three-point bending tests at the lower shelf of their ductile-to-brittle transition curve. Afterward, the fracture surfaces and their cross-sections were analysed to investigate the cleavage initiation and propagation micromechanisms and identify the most critical microstructural features. Therefore, this work establishes the relationship between microstructure, fracture toughness and cleavage micromechanisms in the most critical HAZs of an S690 high strength steel. As a result, a microstructure-based failure criterion for the CGHAZ and ICCGHAZ is developed, allowing the prediction of their fracture behaviour at low-temperature applications concerning structural safety. Moreover, the comprehensive qualitative and quantitative microstructural and fracture data presented in this paper represents the required data for modelling the continuum-level properties of welded structures. Thus, this work can assist in the prediction of fracture behaviour of actual welded structures of high strength steels.

2. Materials and methods

The commercially available 80 mm thick quenched and tempered S690 high strength steel used in this study was previously comprehensively characterised in terms of microstructure and cleavage fracture behaviour [11,16]. The mid-thickness of this steel plate was found to represent the lowest cleavage fracture toughness and, therefore, was chosen for further investigation of welded heat-affected zones. The chemical composition of the middle section of the S690QL high strength steel plate is given in Table 1. The content range of elements referred as "Other" are in accordance with the standard EN 10025-6 (maximum wt. % of Mn:1.7, Ni: 4.0, Cr: 1.5, Nb: 0.06, P: 0.02, N: 0.015, S: 0.01, and B: 0.005) [17].

The microstructures of CGHAZ and ICCGHAZ were created via Gleeble-1500 thermo-mechanical simulator. The thermal profile to simulate the CGHAZ was experimentally obtained from an actual gas metal arc welding (GMAW) procedure with a heat input of 2.2 kJ/mm. First, the material is heated at 210 °C/s up to 1300 °C and held for 2 s. Subsequently, the material is cooled down at 25 °C/s from 1300 to 800 °C, 17 °C/s from 800 to 500 °C, and 6 °C/s to room temperature (Fig. 1 (a)). The same heating and cooling conditions were used for the subsequent thermal cycle of the ICCGHAZ at peak temperatures of 750 °C and 800 °C (Fig. 1 (b)). The temperatures of start (Ac1) and finish (Ac3) of austenite formation were determined by dilatometry as 750 °C and 910 °C, respectively, under the heating rate of 210 °C/s. These thermal profiles were used to perform Gleeble thermal treatments on samples for microstructural characterisation, tensile and fracture testing.

Samples for microstructural characterisation, 80 mm long – parallel to the rolling direction – with 6 mm diameter, were heat treated with the schedules of Fig. 1. Subsequently, the samples were prepared metallographically and etched with Nital 5% for microstructural analysis. Microstructures were observed via scanning electron microscopy (SEM), energy dispersive spectroscopy (EDS) and electron backscatter diffraction (EBSD). In order to accurately identify and quantify M-A constituents, EBSD analysis was used. EBSD data was acquired on a Helios G4 PFIB SEM using a current of 3.2 nA and accelerating voltage of 30 kV, a tilt angle of 70° using TEAM EDAX software, and was post-processed with EDAX-TSL-OIM AnalysisTM v7 software. High and low magnifications were used for M-A characterisation and quantification (step size 0.025 μm) and for prior austenite grain size measurement (step size 1 μm), respectively. In the EBSD scans for the M-A study, the retained austenite was distinguished from the matrix by its FCC crystal structure, while martensite was identified by its clusters of randomly indexed points in the inverse pole figures (IPF) due to its low image quality (IQ), resultant from the high density of defects and the lattice distortion. In this case, the poor indexation is used to identify and quantify the M-A constituents. Therefore, no clean up procedure was performed. To quantify the M-A constituents, the first post-processing step for EBSD data is, for each analysed area, to generate a new data set with the points from the original data set that deviate more than 5° from their neighbours – the randomly indexed points. However, one should be aware that falsely indexed points from the uncertainties in the Kikuchi pattern may be present (e.g., overlapping patterns at grain boundaries) and may lead to inaccurate M-A identification and quantification. These two, randomly (from martensite) and falsely indexed points, can be distinguished by their image quality (IQ). While martensitic areas have lattice

Table 1
Chemical composition of mid-thickness S690QL.

wt.(%)					
Fe	C	Si	Al	Mo	Other
Bal.	0.160 ± 0.001	0.30 ± 0.03	0.080 ± 0.011	0.29 ± 0.02	Mn, Ni, Cr, Nb, P, N, S, B

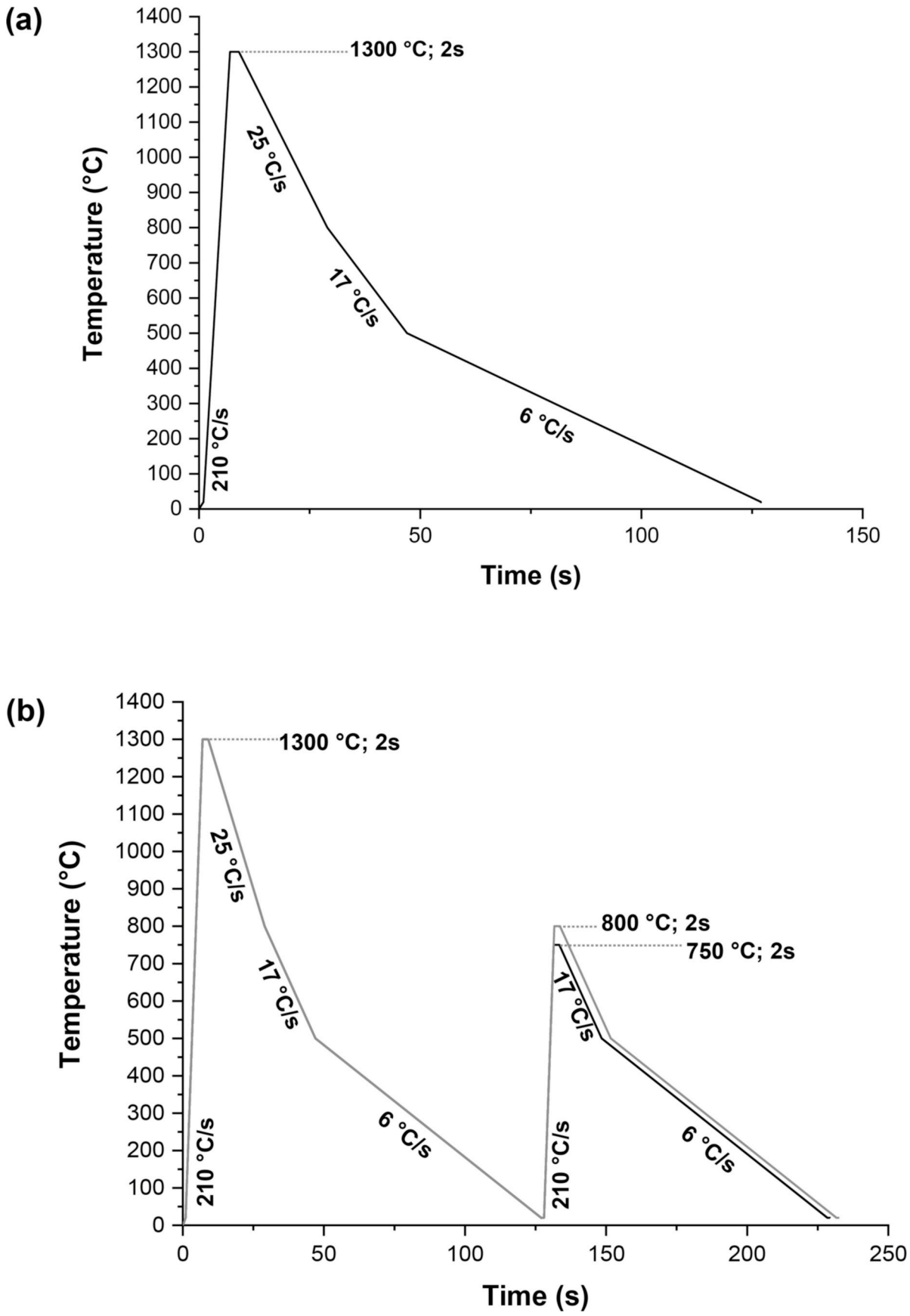

Fig. 1. Gleeble thermal profiles for (a) CGHAZ and (b) ICCGHAZ 750 °C and 800 °C.

distortions and, consequently, low IQ, falsely indexed points do not have a low IQ. Then, points with high IQ were excluded. The threshold between low and high IQ was defined by comparing the grey-scale representation of IQ and the IPF. Afterward, the maps with martensitic areas were overlapped with the phase maps, allowing for the quantification of M-A constituents. For the prior austenite grain (PAG) size measurement, the PAGs were reconstructed via ARPGE software [18], in automatic mode using quadruplets with tolerance for parent grain nucleation and growth of 3° and 6°, respectively. The reconstructed data was post-processed in the TSL-OIM Analysis™ v7 software where the distribution of minor (width) and major (length) axis was acquired and the weighted average grain dimensions were calculated.

To measure the chemical composition of segregation bands Electron Probe Micro Analysis (EPMA) with a JEOL JXA 8900R microprobe was used, with an electron beam with energy of 10 keV and beam current of 200 nA employing Wavelength Dispersive Spectrometry (WDS). The measurements were done through line scans along a 300 μm line in increments of 3 μm. The line scan initiates and ends at points located outside the investigated segregation band, and both points are chosen approximately 150 μm from the centre of the band. Micro-Vickers hardness measurements, loads of 3 kgf (30 N) and 0.025 kgf (0.25 N), were performed for the different studied HAZ, providing overall hardness and individual hardness of the most predominant phase present in each HAZ, respectively.

Tensile specimens (Fig. 2) perpendicular to the rolling direction were heat treated, and a homogeneous simulated microstructure was obtained along 10 mm of the gauge length. Then, the cross section of the original tensile specimen was reduced by 50% (Fig. 2) to achieve the highest stress in this length and, consequently, ensure that the failure occurs within the simulated material. A set of three specimens per heat treatment were tested under a crosshead displacement of 0.2 mm/s and at room temperature using an Instron 100 kN tensile rig. Afterward, the properties were converted to − 40 °C according to the BS7910:2013 + A1:2015 standard [19].

The fracture toughness was assessed via three-point bending tests using sub-sized single edge-notched bending (SENB) specimens (Fig. 3). Between 5 and 10 SENB, T-L (crack propagation direction parallel to the rolling direction (RD)) specimens were heat treated via Gleeble resulting in a homogeneous microstructure along 5 mm of the specimen's centre. Next, the notch was machined by electrical discharge machining in the specimen's centre. The crack/width ratio (a/W) of all specimens is 0.5, and the tests were carried out according to ISO 12135 standard [20]. The crack tip opening displacement (CTOD) parameter was used in this study as a measure of toughness. As the scope of this project is to study cleavage fracture, it is of interest to perform the tests at a temperature below the lower transition region of the ductile-to-brittle transition. The tests were performed at − 40 °C, a temperature at which the cleavage fracture is dominant for all analysed simulated HAZ, by immersing the specimen in liquid nitrogen, at a displacement rate of 2 mm/s using a 350 kN MTS 858 servo-hydraulic test rig. During the test, the crack mouth opening displacement (CMOD) was measured by means of a clip gauge. Note that specimens were initially immersed in liquid nitrogen at −196 °C and then placed between the anvils of the hydraulic test machine, allowing it to warm up slowly, as monitored by a mounted thermocouple. At reaching the test temperature, the load application was triggered. Afterward, to identify the microstructural features playing a role affecting cleavage initiation and propagation

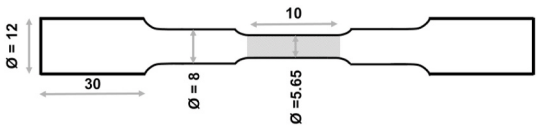

Fig. 2. Tensile specimen of HAZs simulated material. The homogeneous heat-treated area is represented in grey. All dimensions are in mm.

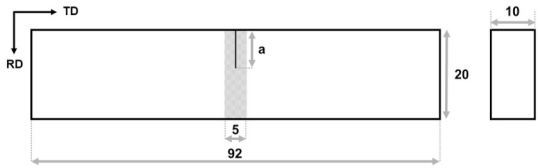

Fig. 3. Dimensions of sub-sized SENB specimens used in fracture toughness tests. The 5 mm homogeneously heat treated region is represented in grey. All dimensions are in mm. RD stands for rolling direction and TD for transverse direction.

micromechanisms, the fracture surfaces were investigated via SEM/EDS and their transverse section by SEM and EBSD, respectively. Note that the analysed transverse section is near the initiation position and, therefore, the area with highest stress. Detailed information on the preparation of the transverse section of fracture surfaces for EBSD analysis is described in Ref. [16].

3. Results

3.1. Microstructural characterisation of HAZs

Figs. 4–6 show the microstructures of the simulated CGHAZ, ICCGHAZ 750 °C, and ICCGHAZ 800 °C, respectively. As can be seen, all investigated HAZs have a complex microstructure composed of a mixture of phases. The CGHAZ is composed of fresh martensite (M), auto-tempered martensite (ATM), and coalesced martensite [21] (indicated by white arrows). For both ICCGHAZ 750 °C and ICCGHAZ 800 °C, the microstructure includes fresh martensite (M), auto-tempered martensite (ATM), bainitic ferrite (BF), granular bainite (GB), and polygonal ferrite (PF). Furthermore, a necklace structure at the prior austenite grain (PAG) boundaries is observed in the ICCGHAZ 750 °C and 800 °C (Figs. 5(a) and Fig. 6(a)). The same structure is also often observed inside the PAG. From SEM investigation, this fine structure is characterised as being composed of auto-tempered martensite.

Fig. 7 exhibits the phase fractions for the base material and the HAZs. Bertolo et al. [11] reported the presence of tempered martensite (TM), tempered bainite (TB) and ferrite (F) in the base material, with TB representing the majority, followed by TM. Nanohardness measurements showed that tempered martensite and tempered bainite, which make up more than 90% of the base material, present similar properties [11]. For the HAZs, the phases that are found in the majority are auto-tempered martensite for the CGHAZ, 90%, and granular bainite for the ICCGHAZ 750 °C and ICCGHAZ 800 °C, 70% and 80%, respectively.

Furthermore, the material subjected to different thermal profiles

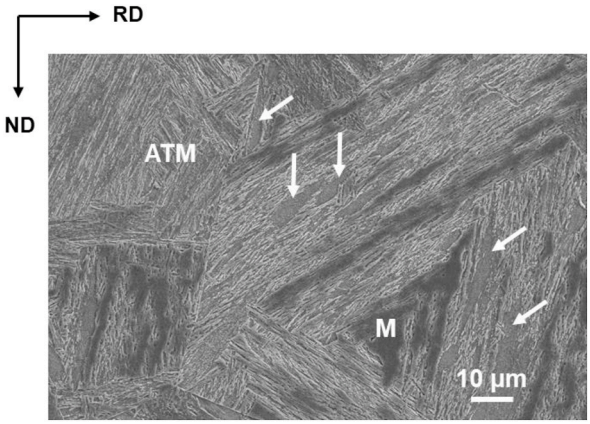

Fig. 4. SEM micrographs of CGHAZ showing fresh martensite (M) and auto-tempered martensite (ATM). The white arrows indicate areas of coalesced martensite. ND stands for normal direction.

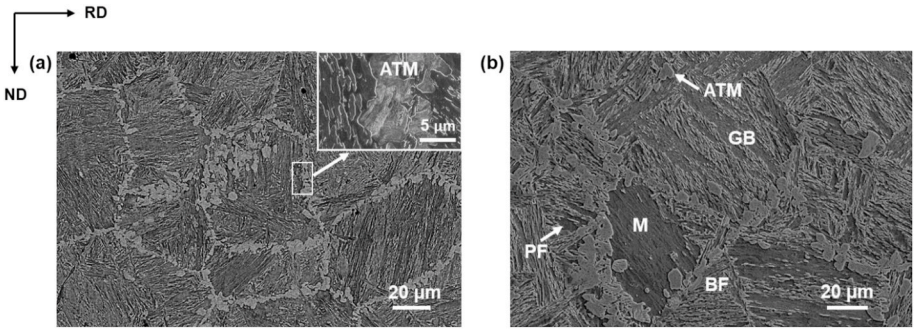

Fig. 5. SEM micrographs of the ICCGHAZ 750 °C showing (a) the necklace structure at prior austenite grain boundaries mainly composed of auto-tempered martensite (ATM) and (b) the presence of fresh martensite (M), auto-tempered martensite (ATM), granular bainite (GB), bainitic ferrite (BF), and polygonal ferrite (PF).

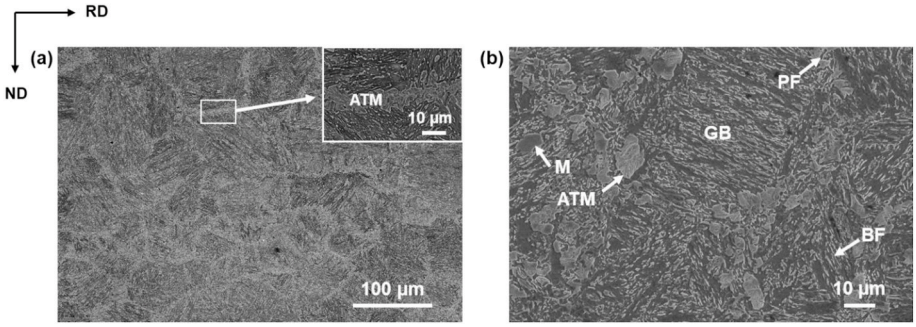

Fig. 6. SEM micrographs of the ICCGHAZ 800 °C showing (a) the necklace structure at prior austenite grain boundaries mainly composed of auto-tempered martensite (ATM) and (b) the presence of fresh martensite (M), auto-tempered martensite (ATM), granular bainite (GB), bainitic ferrite (BF), and polygonal ferrite (PF).

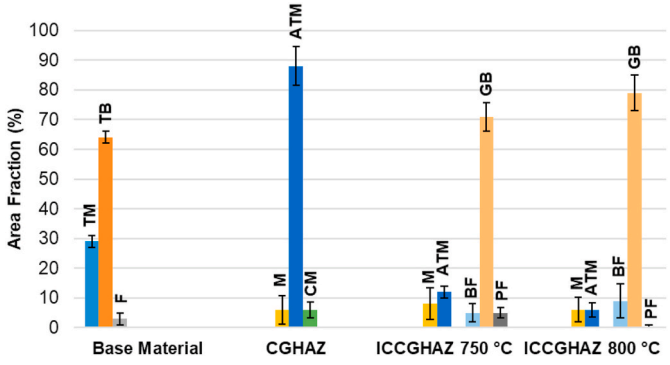

Fig. 7. Phase fractions for the base material, CGHAZ, ICCGHAZ 750 °C, and ICCGHAZ 800 °C. TM stands for tempered martensite, TB for tempered bainite, F for ferrite, M for martensite, ATM for auto-tempered martensite, CM for coalesced martensite, BF for bainitic ferrite, GB for granular bainite, and PF for polygonal ferrite.

retained the centreline segregation bands parallel to the rolling direction, which was previously observed in the middle section of the base material [11]. Table 2 shows the maximum elemental content measured by EPMA inside the segregation bands for the base material and the CGHAZ, ICCGHAZ 750 °C, and ICCGHAZ 800 °C. It should be noted that contrary to the base material where microstructural differences (e.g., grain size) were observed inside and outside the segregation bands, no significant microstructural differences were found in the different HAZs related to the presence of segregation bands. This is possibly related to the decreased degree of segregation of Mn, Cr, and Mo after the thermal cycles in the simulated HAZs, except for the ICGHAZ 750 °C where the Mo content was slightly increased. In the base material, these were the

Table 2
Maximum elemental content (wt.%) measured by EPMA inside the segregation bands for the base material and the CGHAZ, ICCGHAZ 750 °C, and ICCGHAZ 800 °C.

Condition	Maximum Elemental Content (wt.%)					
	Mn	Cr	Mo	Si	Ni	C
As-received	2.2 ± 0.3	1.1 ± 0.2	0.8 ± 0.3	0.40 ± 0.04	0.35 ± 0.04	0.29 ± 0.04
CGHAZ	1.64 ± 0.04	0.821 ± 0.002	0.56 ± 0.05	0.37 ± 0.01	0.31 ± 0.04	0.24 ± 0.05
ICGHAZ 750 °C	1.9 ± 0.4	1.10 ± 0.05	1.01 ± 0.15	0.4 ± 0.1	0.3 ± 0.1	0.42 ± 0.05
ICCGHAZ 800 °C	1.9 ± 0.4	1.0 ± 0.2	0.7 ± 0.3	0.45 ± 0.07	0.39 ± 0.04	0.28 ± 0.04

elements that most strongly segregated in the bands [11]. Therefore, the results presented in this work will not make a distinction between outside and inside segregation bands and will be representative of the overall material, including the segregation bands.

Inclusions pre-existing in the base material [11] were also observed in the simulated HAZ. No difference was found in terms of chemical composition, size, and area fraction between the as-received commercial S690QL steel and the simulated CGHAZ, ICCGHAZ 750 °C, and ICCGHAZ 800 °C microstructures. Spherical inclusions – (Mg,Al,Ca)(O), (Mg,Al,Ca)(O,S), and (Mg,Al,Ca,Ti)(O,N) – with a major-axis (diameter) range of 1–5 µm were present in an area fraction around 3.3×10^{-4}. Cubic inclusions – (Nb,Ti,Mg,Ca)(O,C), (Nb,Ti)(C), (Nb,Ti)(C,N), and NbC – with a major-axis (length) range of 1–12 µm were present in all HAZs, with an area fraction around 2.0×10^{-4}. Thermodynamic simulations by ThermoCalc predict dissolution temperatures of 1161 °C for Nb–Ti carbonitrides and of 1754 °C for Al oxides. Although the peak temperature of the simulated thermal profiles is 1300 °C, the Nb–Ti

carbonitrides are not affected. This is because the thermodynamic simulations consider equilibrium conditions for the calculations, while the welding thermal profiles comprise fast heating, short holding time, and fast cooling, which prevent the system from reaching the equilibrium. Hence, the dissolution temperature predicted by ThermoCalc is not effective for this heat treatment. Fig. 8 shows representative examples of spherical and cubic inclusions in the ICCGHAZ 800 °C, also found in the other samples. Note that typical clusters of cubic inclusions and cracks associated with the inclusions themselves and in the inclusion/matrix interface, which were observed in the base material [11], are also present in the HAZ microstructures.

M-A constituents and PAG size, as key microstructural features in HAZ notably contributing to the reduction of fracture toughness, were analysed and quantified. Fig. 9 (a) – (c) illustrate the special distribution, size, and morphology of M-A constituents in the simulated HAZs. Areas that refer to M-A constituents are the ones with austenitic (green) and martensitic regions (dark grey in the image quality map). Austenitic areas not associated with dark grey areas of the image quality map may be misindexed points (e.g., grain boundaries). Moreover, Fig. 9 (d)–(f) show the Kernel Average Misorientation (KAM) maps for the 3rd neighbour, where the blue and red coloured areas are the ones with the lowest and highest KAM levels, respectively. Misorientations within a grain can be attributed to geometrically necessary dislocations (GND) as they contribute to lattice curvature [22]. The larger the KAM value, the larger the density of GND and, therefore, the larger the plastic strain that has occurred during martensite formation [23]. As M-A constituents are also often observed decorating PAG boundaries, EBSD analysis was carried out for accurate characterisation of the necklace structure at PAG of the ICCGHAZs (Fig. 10).

As can be seen, M-A constituents are present in different amounts, shapes and sizes through the different HAZs. Regarding the presence of M-A constituents within the necklace structures of ICCGHAZs, austenite is associated with low image quality areas, likely to be martensite, distributed in their necklace structures at the PAG boundaries (Fig. 10). Hence, the necklace structure at the PAG boundaries in these conditions is composed of auto-tempered martensite and M-A constituents. Furthermore, the KAM maps show that the M-A constituents are areas of high GND density and, consequently, high degree of plastic strain (Fig. 9 (d)–(f)). Nevertheless, note that the KAM level, and consequently, the GND density and the degree of plastic strain, varies depending on M-A morphology. Some M-A constituents have no internal sub-structure (grain boundaries) and the austenitic part is dense (highlighted by yellow ellipses in Fig. 9 (b), (c), and (f)). In this case, the KAM level is low (mostly green colour). On the other hand, there are M-A constituents with internal sub-structures and sparsely distributed austenite (highlighted by black rectangles in Fig. 9 (b),(c), (e), and (f)). For this morphology, the KAM is high (red colour) and the highest values are associated predominantly with the austenitic areas. The presented morphological differences of M-A and their resultant KAM can be clearly seen for the ICCGHAZs.

Table 3 summarises the area fraction of M-A constituents for each HAZ, their respective average M-A length, and their number fraction of slender and small M-A constituents. The remainder represents blocky and large M-A constituents, respectively. An M-A constituent is considered slender if the aspect ratio is larger than 4. Else, it is considered blocky. Regarding the size, it is considered small if the M-A length is smaller than 1 μm. Else, it is considered large. These values were defined based on the distribution of morphologies and sizes for all investigated areas (See Supplementary Fig. S1).

The quantitative analysis (Table 3) indicates that the ICCGHAZ 750 °C stands out with the highest volume fraction of M-A, 14%, followed by the ICCGHAZ 800 °C, 6%, and the CGHAZ with the lowest area fraction, 4%. The CGHAZ has similar fractions of slender and blocky M-A constituents, while for the ICCGHAZs, the majority is blocky. In terms of size, all materials have a majority of small M-A constituents with average M-A length smaller than 0.9 μm.

The reconstructed PAGs for the simulated HAZ show non-equiaxed grain morphology. For the HAZs, the average ratio of the minor-axis length and the major-axis length ranges from 0.43 to 0.48, similar to the observations for the PAG of the base material [11]. Fig. 11 shows the average grain width and length for the base material and the investigated HAZs. The results indicate that the HAZs have larger PAG size than the base material. Among the HAZs, the CGHAZ has smaller PAG size than the ICCGHAZ 750 °C and ICCGHAZ 800 °C. However, the large scatter present in the ICCGHAZs measurements demonstrates that there is a heterogeneous distribution of grain sizes within the samples, which is not expected to be generated by the intercritical cycle, which is the difference between CGHAZ and ICCGHAZs processing. Therefore, the large scatter indicates that the larger PAG sizes in the ICCGHAZs may be due to a sampling effect, being statistically insufficient for an accurate comparison.

An additional important grain parameter for fracture propagation is the misorientation angle [24]. The misorientation angle distribution for the investigated HAZs is shown in Fig. 12. It can be seen that the curves do not differ through almost the entire angle range, with the exception of certain ranges of misorientation angles (notably 48°–57°). Hence, misorientation angles are not expected to cause significant differences for the different HAZs.

3.2. Mechanical behaviour of simulated HAZs

The micro-Vickers hardness (HV_3) and tensile properties for the simulated CGHAZ, ICCGHAZ 750 °C, and ICCGHZ 800 °C are presented in Table 4 for room temperature (RT) and − 40 °C. The properties of the base material are included for comparison [16]. Note that tensile tests from the base material used standard specimens, without the cross-section reduction as in specimens from the HAZs. As can be seen, the hardness and yield strength are proportional, as expected. In descending order of strength, the HAZs are sorted as CGHAZ, ICCGHAZ 750 °C, and ICCGHAZ 800 °C. To better correlate the overall behaviour

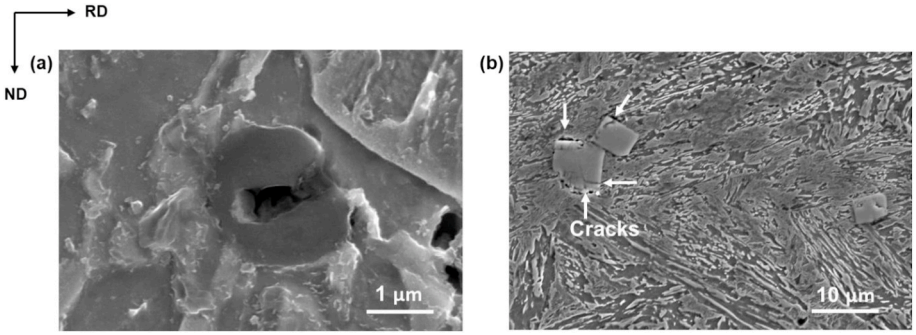

Fig. 8. Representative examples of (a) (Mg,Al,Ca)(O) and (b) (Nb,Ti)(C) and NbC inclusions found in the ICCGHAZ 800 °C. These images are also representative of inclusions found in other simulated HAZs.

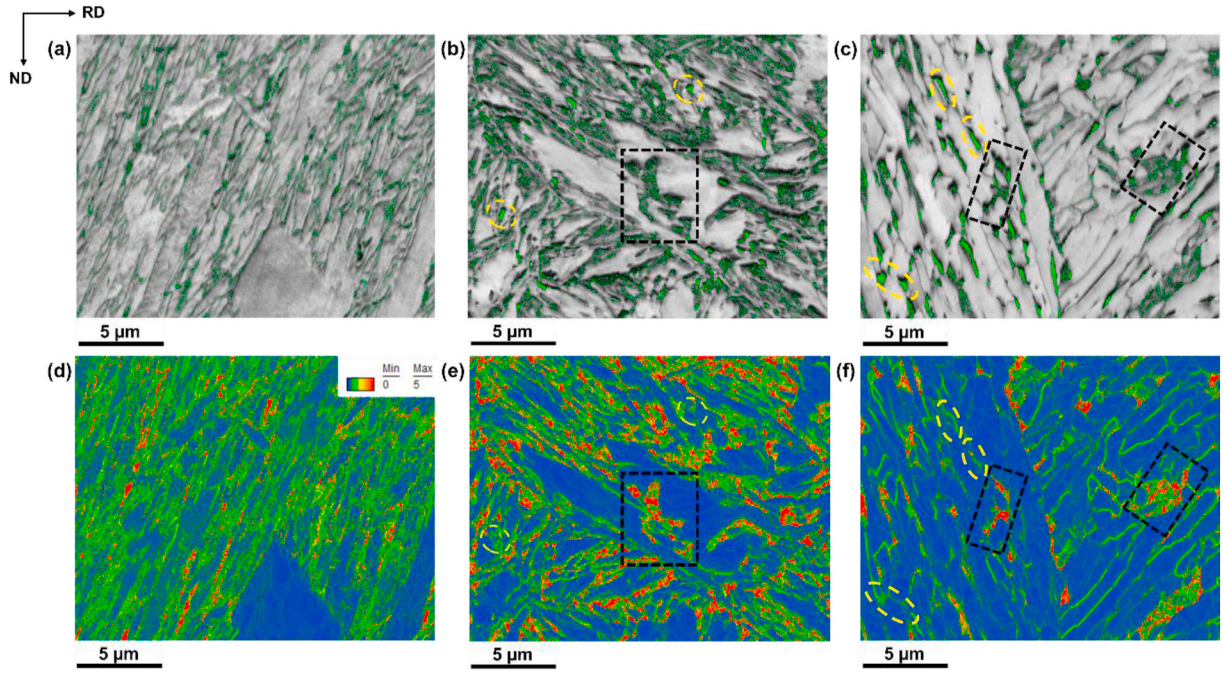

Fig. 9. Combined grey scale image quality map with coloured phase map showing austenite in green and KAM maps for (a,d) CGHAZ, (b,e) ICCGHAZ 750 °C, and (c, f) ICCGHAZ 800 °C. Areas that refer to M-A constituents are the ones with the combined austenitic and martensitic regions (dark grey in image quality map). (For interpretation of the references to colour in this figure legend, the reader is referred to the Web version of this article.)

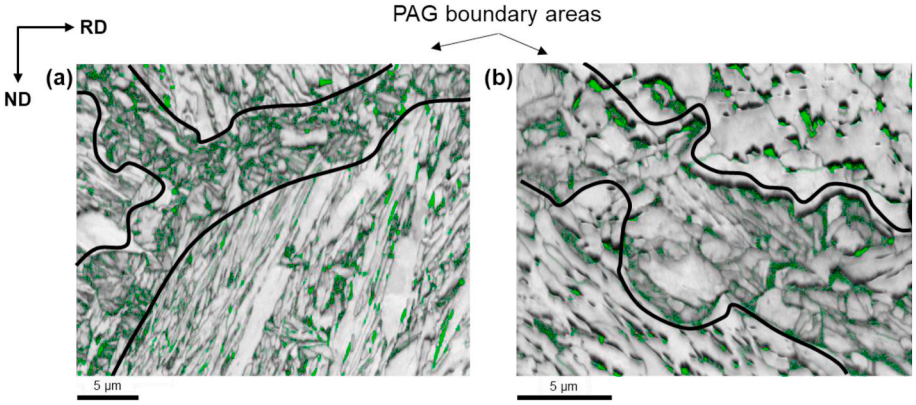

Fig. 10. Combined grey scale image quality map with coloured phase map showing austenite in green for (a) ICCGHAZ 750 °C and (b) ICCGHAZ 800 °C. The black lines delineate the necklace structure found in PAG boundaries. (For interpretation of the references to colour in this figure legend, the reader is referred to the Web version of this article.)

Table 3
Total area fraction of M-A constituent, average M-A length, and the fraction of slender and small M-A for simulated CGHAZ, ICCGHAZ 750 °C, and ICCGHAZ 800 °C.

Condition	Area Fraction of M-A (%)	Morphology (%)	Size (%)	Average M-A Length (μm)
		Slender (aspect ratio >4)	Small (length <1 μm)	
CGHAZ	4 ± 1	53 ± 4	75 ± 5	0.79 ± 0.11
ICCGHAZ 750 °C	14 ± 2	42 ± 10	72 ± 6	0.83 ± 0.04
ICCGHAZ 800 °C	6 ± 1	30 ± 12	75 ± 10	0.74 ± 0.13

of the HAZs and their microstructure, the hardness of the predominant phases of each HAZ was measured ($HV_{0.025}$). The dominant phase in CGHAZ, auto-tempered martensite, is much harder than the dominant granular bainite in the ICCGHAZs.

Fig. 13 (a) displays the average CTOD and the standard deviation from the average for the base material and simulated CGHAZ, ICCGHAZ 750 °C, and ICCGHAZ 800 °C tested at − 40 °C. For context, with a yield strength of 1000 MPa (representative of CGHAZ at −40 °C), a CTOD of 0.02 mm and 0.10 mm correspond to a K_{Ic} of approximately 60, and 130 MPa $m^{1/2}$, respectively. As expected, the HAZs have lower fracture toughness than the base material. The fracture toughness difference between the CGHAZ and ICCGHAZs 750 °C and 800 °C is significant. The CGHAZ shows the lowest CTOD values, followed by the ICCGHAZ 800 °C and the ICCGHAZ 750 °C, where the latter two have similar toughness. Note that the calculation of the CTOD values is influenced by the occurrence of pop-ins in the load-displacement curves. Contrary to the base material, multiple pop-in behaviour was observed in the

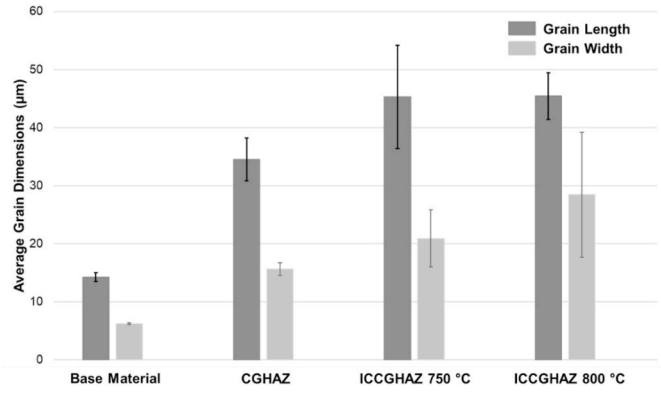

Fig. 11. Average grain width and length of PAG and their standard deviation from the mean for base material and simulated CGHAZ, ICCGHAZ 750 °C, and ICCGHAZ 800 °C.

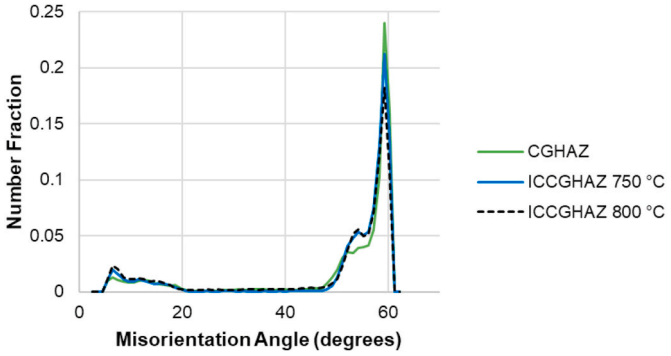

Fig. 12. Misorientation angle distribution for the simulated CGHAZ, ICCGHAZ 750 °C, and ICCGHAZ 800 °C.

Table 4
Micro-Vickers hardness (HV_3 and $HV_{0.025}$) and tensile properties of the base material and the simulated CGHAZ, ICCGHAZ 750 °C, and ICCGHAZ 800 °C at room temperature (RT) and – 40 °C. Hardness measurements are presented for the bulk material and for the HAZ dominant phases of each HAZ.

Condition	Micro-Vickers Hardness (Overall: HV_3 *Predominant Phase: $HV_{0.025}$*)		Yield Strength (MPa)		Tensile Strength (MPa)	
	RT		RT	−40 °C	RT	−40 °C
Base Material	Bulk	270 ± 10	730 ± 5	780 ± 5	850 ± 10	930 ± 10
CGHAZ	Bulk	380 ± 15	950 ± 20	1000 ± 30	1350 ± 50	1470 ± 50
	Auto-tempered martensite	*440 ± 50*	–			
ICCGHAZ 750 °C	Bulk	315 ± 5	690 ± 20	740 ± 20	1130 ± 50	1240 ± 50
	Granular bainite	*330 ± 30*	–			
ICCGHAZ 800 °C	Bulk	230 ± 5	660 ± 10	710 ± 10	1060 ± 30	1160 ± 30
	Granular bainite	*330 ± 10*	–			

CGHAZ and ICCCGHAZs in the bending tests (86%, 17 out of 22 SENB specimens, showed multiple pop-ins). Pop-ins are seen in load-displacement curves as discontinuities as a consequence of a sudden load drop accompanied by an increase in displacement, followed by an increase in load. Fig. 13 (b) shows one load-displacement curve for each HAZ as examples of the multiple pop-in behaviour. The curve for the base material is added for comparison. The perception on the significance of the pop-ins in the determination of fracture toughness, CTOD, varies in literature. The significance of a pop-in can be quantified by a parameter P, which represents the cumulative increase in crack size and compliance due to prior pop-ins and the pop-in being analysed and can be directly determined from the experimental data. Knowing that the compliance is the inverse of stiffness, P_n of the nth pop-in can be determined by

$$P_n = 1 - \frac{S_n^l}{S_1^u} \quad (1)$$

where, S_1^u is the stiffness of the material at the first pop-in considering the upper force value, and S_n^l is the stiffness at the nth pop-in considering the lower force value. More details on P and its calculation can be found in the ISO 12135 [20] standard.

On the one hand, according to the ISO 12135 [20] standard, a pop-in should be taken as critical CTOD point (point which the data is considered as maximum force and displacement for CTOD calculation) if the ratio between the force drop and the maximum force at the pop-in is smaller than P. On the other hand, the ASTM E−1820 [25] considers the pop-in as the critical CTOD point if P is larger than 5%. In the present study we follow the ASTM E−1820 [25] standard and evaluate the significance of a pop-in as $P > 5\%$, since the ISO 12135 standard [20] would result in an overly conservative analysis. In the majority of the specimens, all pop-ins exceeded 5%, where 90% presented $P > 20\%$.

3.3. Microstructural features affecting cleavage fracture in HAZs

3.3.1. Cleavage initiation

Contrary to the base material, clear river lines were not observed on the fracture surface of HAZs. This suggests the presence of multiple initiation sites. As a result, the identification of the initiation sites was challenging, and the fractography at most indicates likely initiation sites. Fig. 14 shows a representative fractographic image of CGHAZ. Fractographic images for the ICCGHAZ 750 °C and ICCGHAZ 800 °C are shown in the Supplementary Fig. S2 and Fig. S3. As can be seen, particles that resemble M-A constituents are present at cleavage facets where river lines appear to be converging.

3.3.2. Cleavage propagation

The cleavage crack propagation of CGHAZ, ICGHAZ 750 °C, and ICGHAZ 800 °C was investigated through SEM directly on the fracture surface and by SEM and EBSD on their transverse section. All simulated HAZs presented the same propagation characteristics. Fig. 15 (a) shows the inverse pole figure (IPF) of the fracture surface profile of an SENB specimen of the simulated CGHAZ as an example. Additionally, prior austenite grains involved in the propagation process are individually analysed (Fig. 15 (b)–(g)). The prior austenite and the martensite phases for the HAZs follow the Kurdjumov-Sachs (K–S) crystallographic orientation relationship. The K–S orientation relationship has 24 variants that can be separated into four groups where variants in each group share the same habit plane and form a packet [26]. Packets consist of blocks that share the same habit plane. The different colours in Fig. 15 (c), (e), and (g) represent different variant groups and, therefore, also represent different packets. Each packet is composed of three blocks of different Bain variants. The Bain axis is the cube axis in which austenite was compressed to be transformed into martensite [26]. The colours in Fig. 15 (b), (d), and (f) represent the Bain variants.

The cleavage fracture in the studied HAZs was found to be transgranular. Note that transgranular fracture was also observed in the ICCGHAZs, meaning that the crack does not progress exclusively through the necklace structure at PAG boundaries. Moreover, the IPF contains evidence of microplasticity due to the presence of dense areas of poorly indexed points along the propagation path as pointed out by

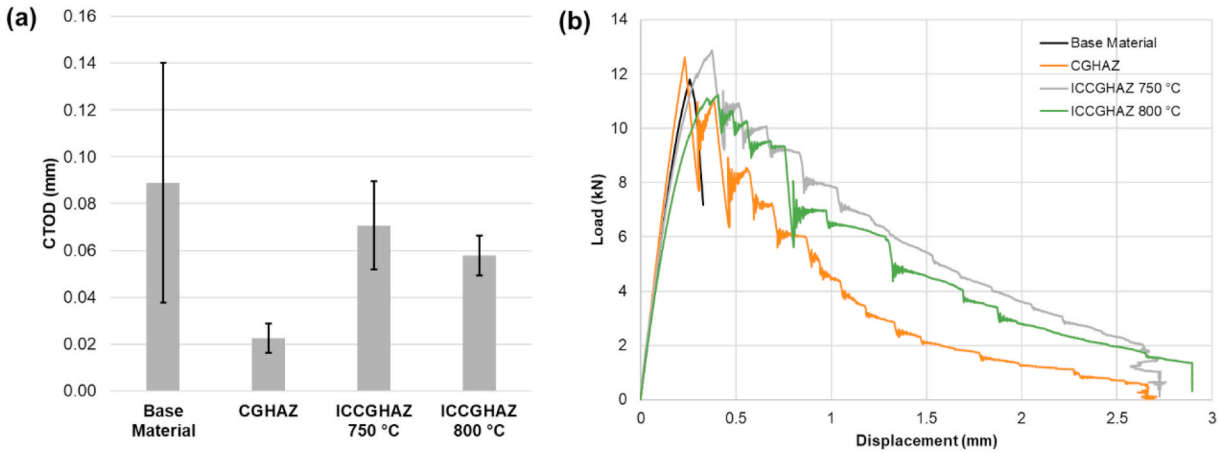

Fig. 13. Plots of (a) CTOD results and their standard deviation from the mean at − 40 °C for the base material and the simulated CGHAZ, ICCGHAZ 750 °C, and ICCGHAZ 800 °C and (b) load *vs.* displacement curve for the base material, CGHAZ, ICCGHAZ 750 °C, and ICCGHAZ 800 °C showing the multiple pop-in behaviour observed in the simulated HAZs.

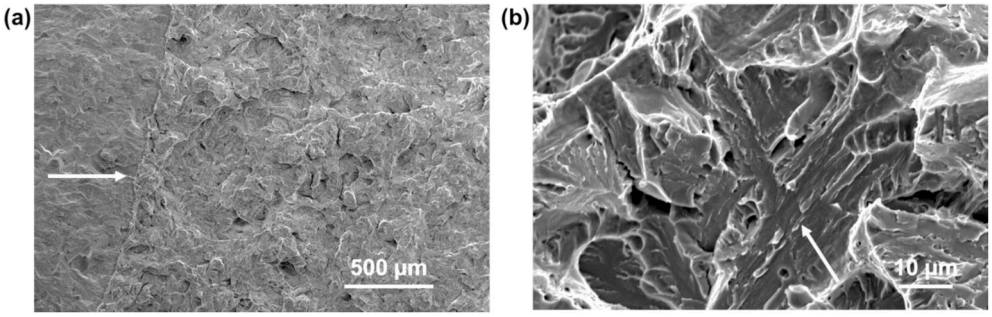

Fig. 14. Fractographic SEM image showing (a) local river lines indicating a likely initiation site in a CGHAZ specimen fractured at −40 °C (CTOD = 0.02 mm) and (b) is a zoom-in of (a) showing a cleavage facet where particles that resemble M-A constituents, pointed out by a white arrow, are likely to have triggered fracture.

Bertolo et al. [16]. Note that accurate data cannot be acquired from these areas. Hence, they are not considered further. Along with the IPF in Fig. 15 (a), 3D crystal lattice cubes are used to analyse the crystal orientations underneath the fracture surface and identify the preferential cleavage crack propagation planes. When determining which plane is parallel to the fracture surface, a tolerance angle of 10 °C is applied. Green and red circles inside the 3D cubes indicate that {100} and {110} planes are aligned parallel to the fracture plane, respectively. As can be seen, the study of the fracture profile shows that {100} and {110} are the most favourable cleavage planes in the CGHAZ. The same is observed for the ICCGHAZ 750 °C and ICCGHAZ 800 °C. Similarly to the base material [16], high-angle grain boundaries, such as PAG boundaries, are observed to deflect the crack, and packets and blocks also play a strong role in diverting the crack when the neighbouring sub-structure has a different Bain axis. However, in some cases, different neighbouring Bain axes cause no or slight crack deflections. Wang [27] explained that this can be related to the thickness of the Bain area (regions of constant colour in Fig. 15 (b), (d), (f)), where thin Bain areas have minor effects on the crack path.

To investigate the role of the M-A constituents in crack propagation, higher magnification EBSD near the crack propagation path was carried out for the investigated HAZs. Fig. 16 shows the image quality map combined with the colour phase map (austenite in green) and the KAM map for the CGHAZ as an example. This area is part of Fig. 15 (a) and refers to the area within the dashed rectangle. The white arrows in Fig. 16 (a) are pointing at some M-A constituents present on the surface. As can be seen, only one M-A constituent is observed to interact with the main crack path. This indicates that M-A constituents do not act as dominant weak links for crack propagation.

4. Discussion

The M-A presence of the CGHAZ, ICCGHAZ 750 °C, and ICCGHAZ 800 °C through thermal welding simulations via Gleeble is in good agreement with other studies [6,28]. In the CGHAZ, the material is heated to very high peak temperatures (above Ac_3). Then, the higher the temperature, the higher the degree of carbon homogenisation, and the less stable austenite is at room temperature. On the other hand, in the ICCGHAZs, the material is intercritically reheated, between Ac_1 and Ac_3, and partially transformed to austenite, which is enriched with carbon. During cooling, it partially transforms into martensite and it is partially retained at room temperature. Nevertheless, the higher the peak temperature, the less the probability of retaining austenite at room temperature. This is because the equilibrium carbon concentration in austenite decreases with increasing temperature. Then, the maximum fraction of M-A constituent content is usually formed at a temperature around Ac_1 and then it decreases at higher temperatures. This explains the largest area fraction of M-A constituent present in the ICCGHAZ 750 °C, 14%; followed by the ICCGHAZ 800 °C, which have less than half of this fraction, 6%; and the CGHAZ, 4%. The necklace structure observed at the PAG boundaries of the ICCGHAZs is formed upon heating above Ac_1, where austenite preferentially nucleates at PAG boundaries. During the subsequent cooling, austenite is partially retained and the rest is transformed to martensite and auto-tempered due to high martensitic start temperature [29]. Another microstructural change observed in the simulated HAZs compared to the base material is the prior austenite grain coarsening, widely reported in the literature [30,31].

According to many authors [5,32,33], the ICCGHAZs present lower

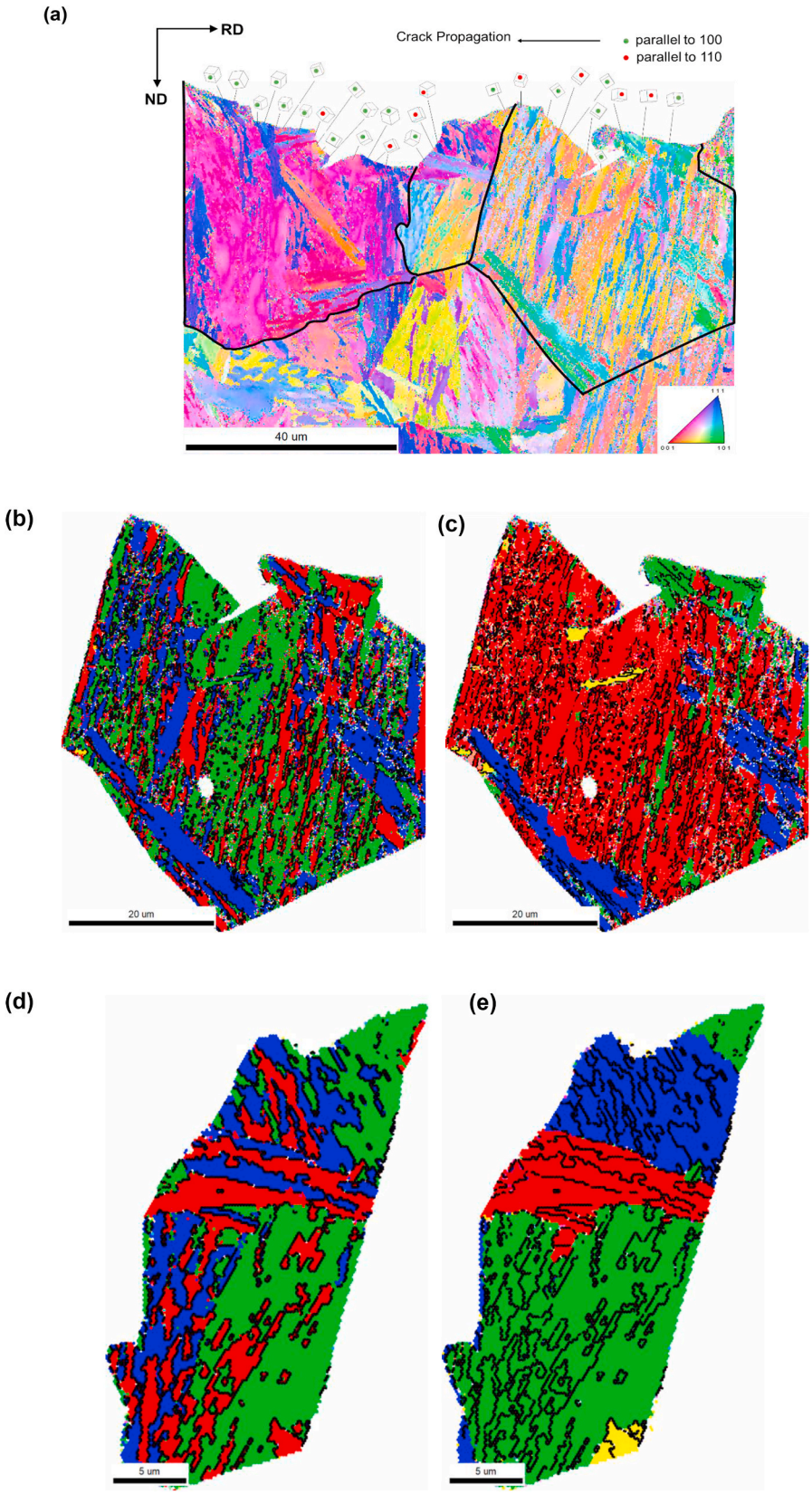

Fig. 15. Fractographic profile of the fractured CTOD specimen of the simulated CGHAZ presented as (a) Inverse Pole Figure, (b) and (c) are an individual PAG located at the right-hand side of (a), (d) and (e) an individual PAG located at the centre of (a), and (f) and (g) an individual grain located at the left-hand side of (a). The colours in (b), (d), and (f) represent different Bain variants, while the colours in (c), (e), and (g) represent the different groups of K–S variants. Thin black lines are high-angle (misorientation larger than 15°) grain boundaries and the thick black contour in (a) is the PAG boundary. (For interpretation of the references to colour in this figure legend, the reader is referred to the Web version of this article.)

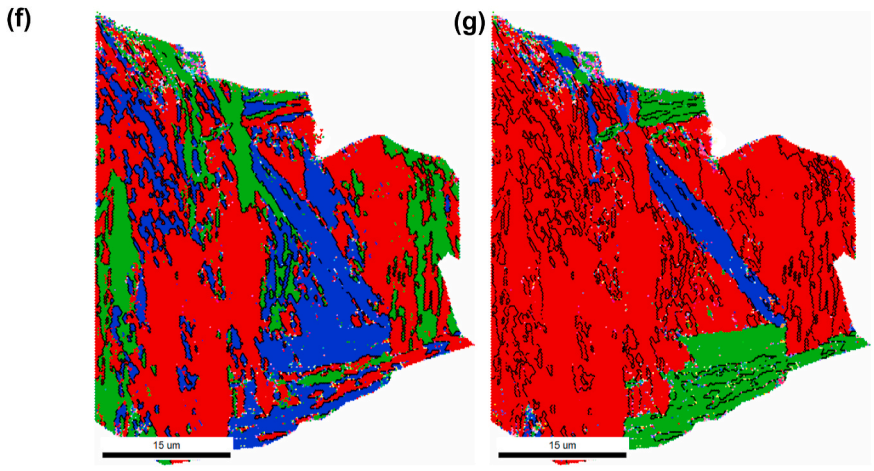

Fig. 15. (*continued*).

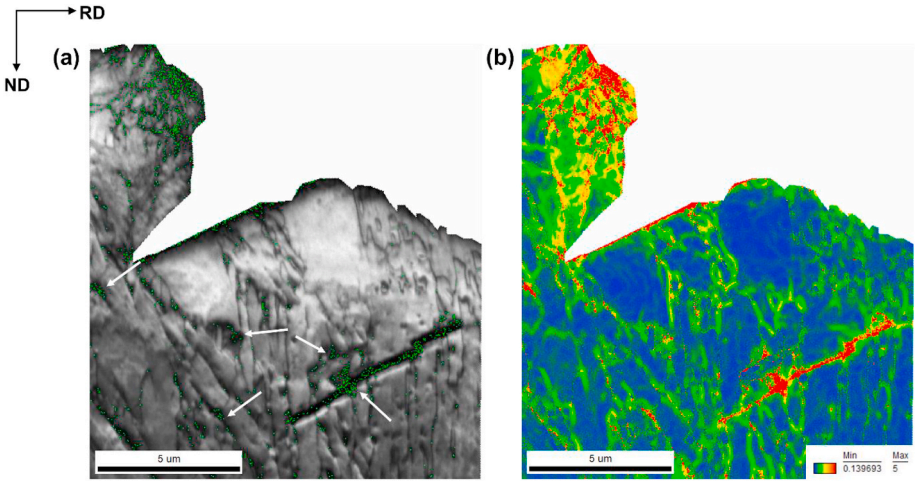

Fig. 16. Fractographic profile of a simulated CGHAZ CTOD specimen presented as (a) combined grey image quality map and coloured phase map where austenite is represented as green and (b) Kernel average misorientation (KAM) map. The white arrows in (a) are pointing out to some M-A constituents present on the surface. (For interpretation of the references to colour in this figure legend, the reader is referred to the Web version of this article.)

toughness than the CGHAZ. They attribute the main loss of toughness in the intercritically reheated zones to M-A constituents, that are present in a larger size, higher fraction, and also along PAG boundaries in a necklace-like form. Moreover, phases such as bainitic ferrite and granular bainite, often observed in ICCGHAZs, are also indicated as unfavourable microstructure constituents as they have low toughness [5]. The abovementioned microstructural characteristics that differentiate CGHAZ from ICCGHAZ and make the latter more prone to brittle fracture are also observed in the HAZs of the present study. However, in the present work, the CGHAZ exhibits the lowest fracture toughness. To understand the differences between the HAZs, the fracture surfaces of the CTOD specimens were analysed. Contrary to the base material (plate's mid-thickness) – tested at −100 °C at different a/W ratios, which covers the lower transition and lower shelf regimes of the ductile-to-brittle transition curves [16] – where cubic Nb-rich and oxide inclusions are observed as cleavage crack initiators, the fracture surface analyses of the HAZs indicate that the microstructural feature triggering fracture is likely to be M-A. This happens despite Nb-rich and oxide inclusions being larger, which increases vulnerability to fracture, and Nb-rich inclusions being harder, which makes it more brittle and prone to fracture than M-A constituents. According to the KAM maps, the M-A constituents are the areas with the highest KAM values, indicating a high dislocation density and formation of dislocation pile-ups. Consequently, high stresses are induced in M-A constituents [34]. Under the combined applied stress on the structure and the phase-transformation induced stresses during the heat treatment, M-A constituents are more readily cracked than Nb-rich inclusions. Note that residual stresses between the Nb-rich inclusions and the steel matrix are also usually present in steel plates due to thermal expansion [35]. Nevertheless, these residual stresses are probably relieved in the welding thermal cycles. Still, if the difference in fracture behaviour between CGHAZ and ICCGHAZs would be caused by crack initiation in M-A constituents, the ICCGHAZ 750 °C would represent the worst case as it has the largest M-A fraction and, therefore, a higher density of sites to locally initiate cracks. Instead, the ICCGHAZ 750 °C represents the HAZ with the highest fracture toughness in this study. This is related to the dimensions of M-A constituents. According to the Griffith criterion [36], the critical cleavage fracture stress is inversely proportional to the square root of the crack length. In this work, as M-A constituents are observed as crack initiators, the crack length can be assumed equal to the M-A constituent size. Hence, if the M-A size is at least equivalent to the length required for the critical event, the crack propagates in an unstable manner until final fracture. Otherwise, the crack would propagate stably until reaching the size of the critical crack through the particle/matrix interface, into the matrix and across the matrix/matrix interface [34,37]. In the present study, the M-A constituents are predominantly small (70–75% is smaller than 1 μm

in all HAZs), which is likely not sufficient to attain the local cleavage fracture stress. Hence, the matrix and its properties also influence the fracture toughness due to the crack propagation step. This explains the tougher behaviour of ICCGHAZs compared to the CGHAZ. The highest hardness and tensile properties of the CGHAZ are due to the auto-tempered martensite along with the smallest PAG dimensions. Due to the fast welding thermal cycles, the degree of auto-tempering is very limited and the auto-tempered martensite has properties comparable to fresh martensite rather than to significantly tempered martensite. For instance, the CGHAZ is harder and stronger than the base material composed of tempered martensite and tempered bainite. The ICCGHAZs, in turn, have lower hardness and tensile properties than the CGHAZ as a result of their predominant microstructure of granular bainite and larger PAG dimensions. The higher hardness and tensile properties of ICCGHAZ 750 °C compared to the ICCGHAZ 800 °C are likely due to the difference in the M-A constituent content, 14%, and 6%, respectively. Therefore, contrary to the findings in the literature [2–5], the microstructural composition of the HAZ matrix plays a more important role in fracture behaviour than M-A constituents.

The propagation micromechanisms are similar to the ones observed in the base material where cracks propagate in a transgranular manner and the PAG boundaries and packet and block boundaries with different neighbouring Bain axes are the microstructural characteristics effectively diverting the cleavage crack. It is also seen that, different from the studies in the literature [38,39], the necklace structure of tempered martensite and M-A constituents at PAG boundaries are not preferential sites for crack propagation. M-A constituents are also not observed along the crack path of the fracture profile, an indication that they are not playing a significant role in the crack path. This is also supported by the observation that the crack propagates along the {100} and {110} planes, known as preferential cleavage planes in BCC steels [40].

It should however be noted that, contrary to the base material, the HAZs exhibit distinct pop-ins in the load-displacement curves, indicating multiple crack initiations and arrests (Figs. 13(b) and Fig. 17(g)–(i)). According to the literature [41–43], a pop-in is a discontinuity in the load-displacement curve resulting from local unstable crack growth which is subsequently arrested. A crack can be arrested, for instance, by surrounding tougher material or by the initiation of cracks perpendicular to the plane of the initial crack, also called delamination or splitting, and of secondary cracks [41–44]. Usually, the region of the arrested crack can be seen on the fracture surface as well as delamination/splitting. Fig. 17 shows macrographs of the fracture surface, micrographs of the fracture surface at the initiation site indicated by the white arrow (area where the river lines are converging), and the load-displacement curves for the CGHAZ (a, d, g), ICCGHAZ 750 °C (b, e, h), and ICCGHAZ 800 °C (c, f, j), respectively. As can be seen from the macro- and micrographs, there is no sign of delamination/splitting on the fracture surface. The transverse section of the fracture surfaces were also investigated. However, very few secondary cracks were observed, which would not justify the multiple pop-ins. Hence, the surrounding microstructure should be the cause for this behaviour.

To identify potential microstructural features responsible for reducing the crack energy and arresting the crack, EBSD analysis was carried out on secondary cracks on the transverse section of the fracture surface underneath the crack path (Fig. 18). As can be seen, M-A constituents are found along the propagation path of secondary cracks. In some cases, for instance in Fig. 18 (a) point 1, (c) points 1 and 2, and (e) point 1, some M-A constituents are observed to deflect the crack. Note that point 1 in Fig. 18 (e) resembles an M-A constituent, but it is too small compared to the crack width to accurately identify it. Moreover, points 2 and 3 in (e) show a crack initiation and crack arrest in M-A constituents. On the other hand, there are cases where M-A constituents

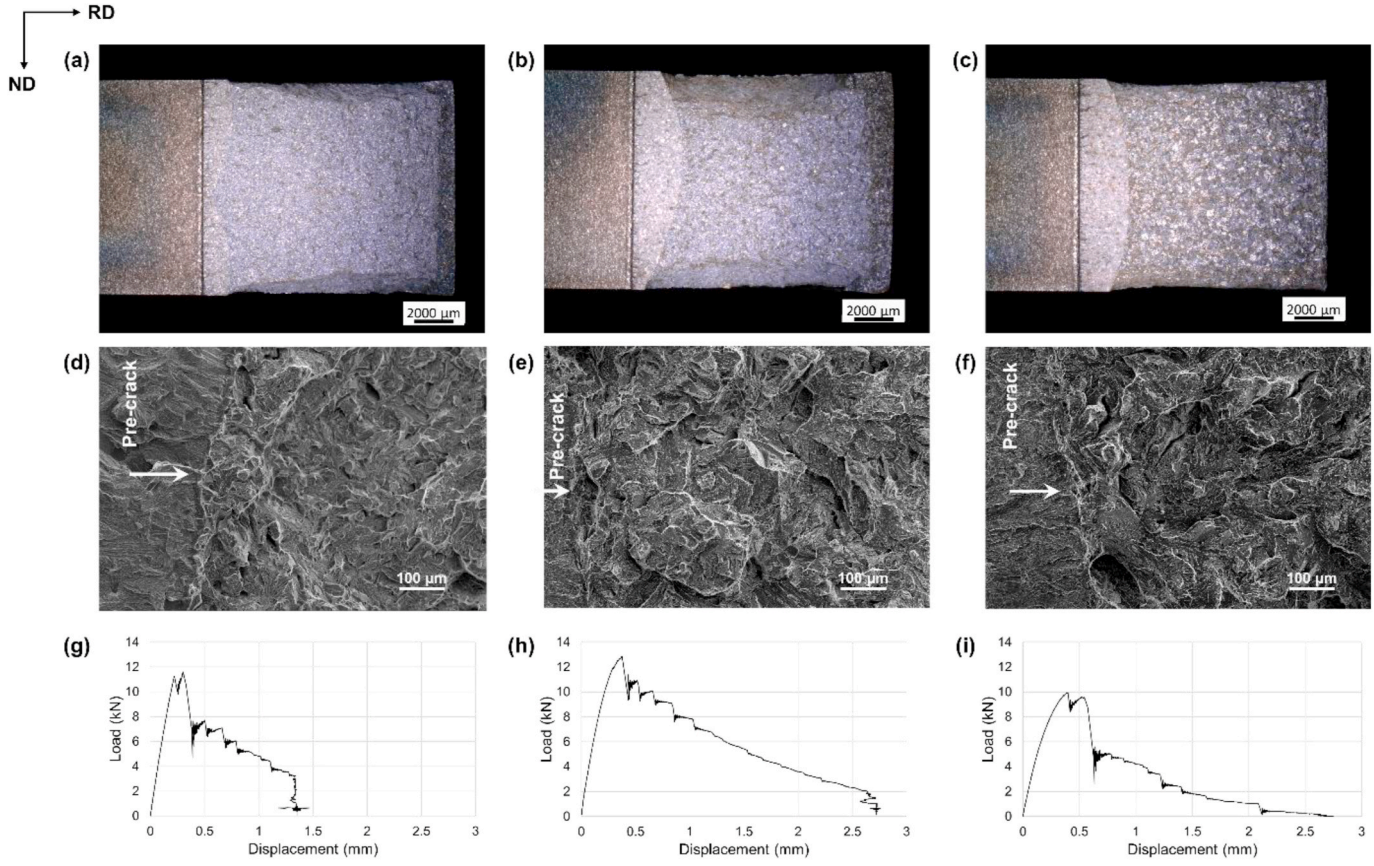

Fig. 17. Macrographs and micrographs of the fracture surface and respective load-displacement curves of (a,d,g) CGHAZ, (b,e,h) ICCGHAZ 750 °C, and (c,f,i) ICCGHAZ 800 °C. The white arrows in the micrographs (d,e,f) are pointing out to the location of the initiation site.

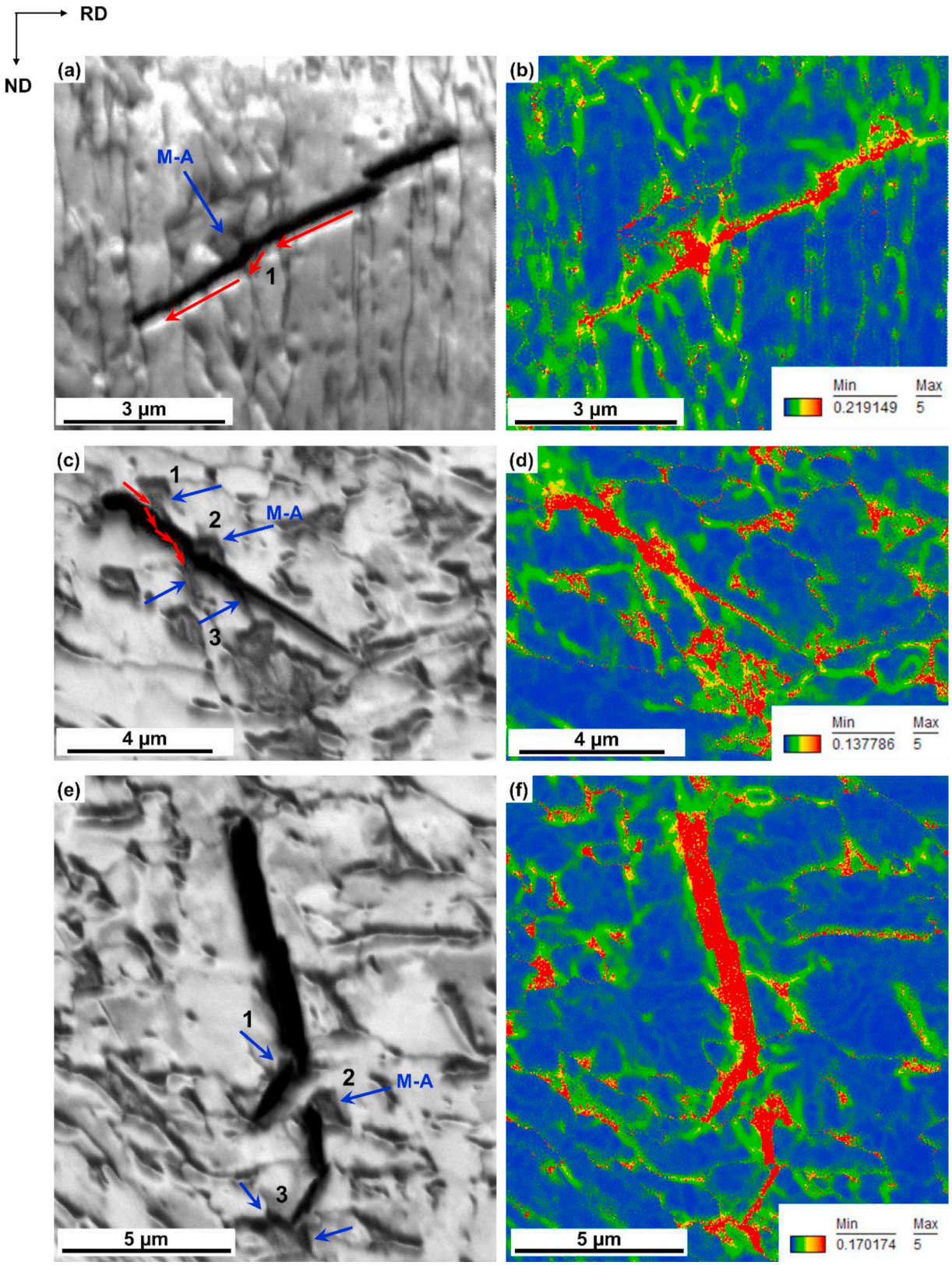

Fig. 18. Image quality and KAM maps of secondary cracks on the transverse section of the fracture surface of (a,b) CGHAZ and (c,d,e,f) ICCGHAZ 800 °C. Blue arrows in (a,c,e) point out to M-A constituents interacting with secondary cracks. The red arrows in (a,c) are used to highlight the crack deflection. (For interpretation of the references to colour in this figure legend, the reader is referred to the Web version of this article.)

do not influence the crack propagation path, as pointed out by point 3 in Fig. 18 (c). The M-A influence on the crack path is attributed to the different KAM distributions. KAM gives semi-quantitative information on geometrically necessary dislocations and, therefore, deformation localizations [23]. The strain located in M-A constituents is a consequence of the residual stresses induced during phase transformation to martensite and the retention of austenite during cooling. As an FCC crystal lattice is more closely packed than BCC, body centered cubic, and BCT, body cubic tetragonal, lattices, compressive stresses are generated in the surrounding matrix material during the transformation from austenite to martensite as a result of volume expansion [4]. Note that the residual stresses developed in actual welds are not present in thermally simulated welds. Then, their possible effect on the stress distribution inside M-A constituents is not considered here. From our observations, M-A constituents present different KAM distributions, depending on their morphology. The M-A constituents with internal substructures and sparse austenitic areas have higher KAM values than M-A constituents with small parts of martensite and dense areas of austenite. These observations are in good agreement with the literature [45]. Hence, when a crack interacts with M-A constituents with high KAM, the compressive stresses at M-A constituents affect the crack tip stress state, reducing the stress intensity and, therefore, its criticality. The reduction of crack-tip stresses due to the interaction of the crack with compressive stresses explains the crack deflections and also the crack arrest events. Furthermore, the literature also shows that the internal sub-structures of M-A constituents include high-angle boundaries, which can also change the direction of a crack or hinder it [45]. As a consequence, M-A constituents with internal sub-structures are potential microstructural features to be responsible for multiple pop-in behaviour. Therefore, it can be concluded that besides high-angle grain boundaries and Bain axes, M-A constituents with internal sub-structures and high KAM are important for the cleavage micromechanisms of HAZs of high-strength steels. Moreover, for macroscopic fracture, when the first pop-in within many, such as for the HAZs under study, is taken as the point of critical CTOD, the result underestimates the material's fracture toughness.

In summary, the fracture process is triggered by M-A constituents, which are too small (less than 1 μm) to reach the stress for unstable crack growth. Then, the crack continues to grow through the matrix until it reaches the critical size Thus, the matrix and its properties strongly influence the fracture toughness. Moreover, M-A constituents, besides acting as crack initiators, are also observed to influence the propagation step. Although they are not preferential crack paths, M-A constituents with internal sub-structures can still deflect and arrest the crack, influencing the crack propagation path. Other features such as PAG boundaries, and packets and block boundaries with different Bain axes are also observed to deflect the crack.

5. Conclusions

The influence of microstructure on cleavage fracture toughness and micromechanisms of fracture in CGHAZ and ICCGHAZs of quenched and tempered S690 high strength steels was studied in this work. The microstructure of CGHAZ, ICCGHAZ 750 °C, and ICCGHAZ 800 °C were studied via different techniques and the fracture behaviour was studied through three-point bending tests at −40 °C. The following conclusions can be made:

1. The ICCGHAZ 750 °C has the highest volume fraction of M-A, 14%, followed by the ICCGHAZ 800 °C, 6%, and the CGHAZ, 4%. In terms of morphology, M-A constituents are found in the form of dense austenitic areas along with a small portion of martensite on one side and with internal sub-structures where austenite is sparsely distributed. The latter presents the highest KAM, meaning that these M-A constituents have high geometrically necessary dislocation density (plastic strain) and compressive stress.
2. M-A constituents are found to trigger the fracture in CGHAZ and ICCGHAZs. However, due to their size (smaller than 1 μm), main cracks initiated from M-A constituents are likely not representing the critical crack length for unstable crack and final fracture. Hence, the matrix also contributes to the crack-growth step. The tougher behaviour of ICCGHAZs compared to the CGHAZ is associated with the matrix and its properties. The highest hardness and tensile properties of the CGHAZ are due to the auto-tempered martensite along with the smallest PAG. The ICCGHAZs, in turn, have lower hardness and tensile properties as a result of their microstructure of granular bainite and larger PAG dimensions.
3. The main crack propagates in a transgranular manner in all investigated HAZs and, therefore, the necklace structure at PAG boundaries of ICCGHAZs is not a preferential propagation path. Likewise, M-A constituents are rarely observed in the main crack path, meaning that these brittle particles do not act as favourable routes for propagation. This is also supported by the observation that the main crack propagates along the {100} and {110} planes. The PAG boundaries and packet and block boundaries with different neighbouring Bain axes are found to effectively divert the cleavage crack.
4. Multiple pop-ins are observed in the load-displacement curves of all investigated HAZs. The analysis of secondary cracks indicates that the M-A constituents with internal sub-structures have high KAM and are able to deflect and arrest secondary cracks. This is related to the reduction of crack-tip stresses due to the compressive stresses inside the M-A constituents and the high-angle boundaries of sub-structures. Hence, M-A constituents with these characteristics are potential features responsible for the multiple pop-in behaviour.

From a statistical and quantitative analysis of the microstructure and the fracture process, this research establishes the role of different microstructural features and parameters on the cleavage fracture micromechanisms of complex, multi-phase CGHAZ and ICCGHAZs of an S690QL high strength steel. Thus, a quantitative and statistical relationship between microstructure and cleavage fracture behaviour is defined, contributing to modelling predictions and, ultimately, the development of a microstructure-based failure criterion. Furthermore, this study brings insight into the microstructural aspects of HAZs to be considered when designing welded joints, which can improve low-temperature toughness of CGHAZ and ICCGHAZs, such as the size and morphology of M-A constituents (smaller than 1 μm and blocky with internal sub-structures) and matrix toughness.

CRediT authorship contribution statement

V. Bertolo: Conceptualization, Methodology, Validation, Formal analysis, Investigation, Resources, Data curation, Writing – original draft, Writing – review & editing, Visualization. **Q. Jiang:** Conceptualization, Methodology, Software, Formal analysis, Resources, Writing – original draft, Writing – review & editing. **M. Terol Sanchez:** Investigation, Data curation, Writing – review & editing. **T. Riemslag:** Investigation, Writing – review & editing. **C.L. Walters:** Conceptualization, Validation, Writing – review & editing, Supervision. **J. Sietsma:** Conceptualization, Validation, Writing – review & editing, Supervision. **V. Popovich:** Conceptualization, Validation, Writing – review & editing, Supervision, Project administration.

Declaration of competing interest

The authors declare that they have no known competing financial interests or personal relationships that could have appeared to influence the work reported in this paper.

Data availability

The raw/processed data required to reproduce these findings cannot

be shared at this time as the data also forms part of an ongoing study.

Acknowledgment

The authors acknowledge the support in the Micro-Tough research project (n. 16350) from the Dutch Research Council (NWO) and the consortium of partners that include Allseas Engineering, Aktien-Gesellschaft der Dillinger Hüttenwerke, Lloyd's Register, The Dutch Ministry of Defence, and TNO. We also acknowledge C. Kwakernaak from the Surfaces & Interfaces group of TU Delft for performing EPMA analysis.

Appendix A. Supplementary data

Supplementary data to this article can be found online at https://doi.org/10.1016/j.msea.2023.144762.

References

[1] V. Popovich, I.M. Richardson, Fracture toughness of welded thick section high strength steels, in: TMS 2015 144th Annual Meeting & Exhibition: Supplemental Proceedings, Springer International Publishing, Cham, 2015, pp. 1031–1038.
[2] S. Lee, B.C. Kim, D.Y. Lee, Fracture mechanism in coarse grained HAZ of HSLA steel welds, Scripta Metall. 23 (1989) 995–1000, https://doi.org/10.1016/0036-9748(89)90284-6.
[3] P. Mohseni, J.K. Solberg, M. Karlsen, et al., Investigation of mechanism of cleavage fracture initiation in intercritically coarse grained heat affected zone of HSLA steel, Mater. Sci. Technol. 28 (2012).
[4] C.L. Davis, J.E. King, Cleavage initiation in the intercritically reheated coarse-grained heat-affected zone : Part I . Fractographic evidence, Metall. Mater. Trans. A 25A (1994) 563–573.
[5] S.G. Lee, B. Kim, S.S. Sohn, et al., Effects of local-brittle-zone (LBZ) microstructures on crack initiation and propagation in three Mo-added high-strength low-alloy (HSLA) steels, Mater. Sci. Eng., A 760 (2019) 125–133, https://doi.org/10.1016/j.msea.2019.05.120.
[6] E. Bayraktar, D. Kaplan, Mechanical and metallurgical investigation of martensite-austenite constituents in simulated welding conditions, J. Mater. Process. Technol. 153 (154) (2004) 87–92, https://doi.org/10.1016/j.jmatprotec.2004.04.021.
[7] S. Kumar, S.K. Nath, Effect of weld thermal cycles on microstructures and mechanical properties in simulated heat affected zone of a HY 85 steel, Trans. Indian Inst. Met. 70 (2017) 239–250, https://doi.org/10.1007/s12666-016-0880-1.
[8] B.C. Kim, S. Lee, N.J. Kim, D.Y. Lee, Microstructure and local brittle zone phenomena in high-strength low-alloy steel welds, Metall. Trans. A 22 (1991) 139–149.
[9] X. Luo, X. Chen, T. Wang, et al., Effect of morphologies of martensite–austenite constituents on impact toughness in intercritically reheated coarse-grained heat-affected zone of HSLA steel, Mater. Sci. Eng., A 710 (2018) 192–199, https://doi.org/10.1016/j.msea.2017.10.079.
[10] Y. Li, T.N. Baker, Effect of morphology of martensite-austenite phase on fracture of weld heat affected zone in vanadium and niobium microalloyed steels, Mater. Sci. Technol. 26 (2010) 1029–1040, https://doi.org/10.1179/026708309X12512744154360.
[11] V. Bertolo, Q. Jiang, S. Scholl, et al., A comprehensive quantitative characterisation of the multiphase microstructure of a thick-section high strength steel, J. Mater. Sci. (2022), https://doi.org/10.1007/s10853-022-07121-y.
[12] J.J. Penagos, J.I. Pereira, P.C. Machado, et al., Synergetic effect of niobium and molybdenum on abrasion resistance of high chromium cast irons, Wear 376 (377) (2017) 983–992, https://doi.org/10.1016/j.wear.2017.01.103.
[13] Y. Wang, Q. Wang, L. Liu, W. Xu, Fracture mode of martensite-austenite constituents containing multiphase steel controlled by microstructural and micromechanical aspects, Mech. Adv. Mater. Struct. 22 (2015) 591–596, https://doi.org/10.1080/15376494.2013.828808.
[14] Huda N Effect of Martensite-Austenite (MA) on Mechanical Properties of X80 Linepipe Steel. University of Waterloo.
[15] M.G. Vassilaros, Fracture Behavior of Ultra-low-carbon Steel Plate and Heat-Affected Zone, 1990.
[16] V. Bertolo, Q. Jiang, U. Tiringer, et al., Cleavage fracture micromechanisms in thick-section quenched and tempered S690 high- strength steels, J. Mater. Sci. (2022), https://doi.org/10.2139/ssrn.4055055.
[17] CEN, NEN-EN 10025-6: Hot Rolled Products of Structural Steels - Part 6: Technical Delivery Conditions for Flat Products of High Yield Strength Structural Steels in the Quenched and Tempered Condition, 2019.
[18] C. Cayron, ARPGE : a computer program to automatically reconstruct the parent grains from electron backscatter diffraction data, J. Appl. Crystallogr. 40 (2007) 1183–1188, https://doi.org/10.1107/S0021889807048777.
[19] BSI, BS7910:2013+A1:2015 Guide to Methods for Assessing the Acceptability of Flaws in Metallic Structures, 2015.
[20] ISO, ISO 12135: Metallic Materials - Unifed Method of Test for the Determination of Quasistatic Fracture Toughess, 2018, 2016.
[21] H. Pous-Romero, H. Bhadeshia, Coalesced martensite in pressure vessel steels, J. Press Vessel. Technol. Trans. ASME 136 (2014) 1–6, https://doi.org/10.1115/1.4026192.
[22] J. Jiang, T.B. Britton, A.J. Wilkinson, Measurement of geometrically necessary dislocation density with high resolution electron backscatter diffraction: effects of detector binning and step size, Ultramicroscopy 125 (2013) 1–9, https://doi.org/10.1016/J.ULTRAMIC.2012.11.003.
[23] M. Calcagnotto, D. Ponge, E. Demir, D. Raabe, Orientation gradients and geometrically necessary dislocations in ultrafine grained dual-phase steels studied by 2D and 3D EBSD, Mater. Sci. Eng., A 527 (2010) 2738–2746, https://doi.org/10.1016/j.msea.2010.01.004.
[24] H. Liu, H. Zhang, J. Li, Thickness dependence of toughness in ultra-heavy low-alloyed steel plate after quenching and tempering, Metals 8 (2018) 1–11, https://doi.org/10.3390/met8080628.
[25] ASTM International, E1820: Standard Test Method for Measurement of Fracture Toughness, 2020.
[26] J.W. Morris Jr., C. Kinney, K. Pytlewski, Y. Adachi, Microstructure and cleavage in lath martensitic steels, Sci. Technol. Adv. Mater. 14 (2013) 1–9, https://doi.org/10.1088/1468-6996/14/1/014208.
[27] X. Wang, Z. Wang, Z. Xie, et al., Combined effect of M/A constituent and grain boundary on the impact toughness of CGHAZ and ICCGHAZ of E550 grade offshore engineering steel, Math. Biosci. Eng. 16 (2019) 7494–7509, https://doi.org/10.3934/mbe.2019376.
[28] E. Bonnevie, G. Ferrière, A. Ikhlef, et al., Morphological aspects of martensite–austenite constituents in intercritical and coarse grain heat affected zones of structural steels, Mater. Sci. Eng., A 385 (2004) 352–358, https://doi.org/10.1016/J.MSEA.2004.06.033.
[29] X.L. Wang, Y.R. Nan, Z.J. Xie, et al., Influence of welding pass on microstructure and toughness in the reheated zone and multi-pass weld of 550 MPa offshore engineering steel, Mater. Sci. Eng., A 702 (2017) 196–205.
[30] M. Shome, O.P. Gupta, O.N. Mohanty, Effect of simulated thermal cycles on the microstructure of the heat-affected zone in HSLA-80 and HSLA-100 steel plates, Metall. Mater. Trans. A Phys. Metall. Mater. Sci. 35 (2004) 985–996, https://doi.org/10.1007/s11661-004-1002-y.
[31] J. Zhang, W. Xin, G. Luo, et al., Significant influence of welding heat input on the microstructural characteristics and mechanical properties of the simulated CGHAZ in high nitrogen V-alloyed steel, High Temp. Mater. Process. 39 (2020) 33–44, https://doi.org/10.1515/htmp-2020-0003.
[32] Z. Zhu, L. Kuzmikova, H. Li, F. Barbaro, Effect of inter-critically reheating temperaure on microstructure and properties of simulated inter-critically reheated coarse grained heat affected zone in X70 steel, Mater. Sci. Eng., A (2014) 8–13.
[33] C. Fu, X. Li, H. Li, et al., Influence of ICCGHAZ on the low-temperature toughness in HAZ of heavy-wall X80 pipeline steel, Metals 12 (2022) 907, https://doi.org/10.3390/met12060907.
[34] J.H. Chen, R. Cao, Micromechanism of Cleavage Fracture of Metals, Butterworth-Heinemann, Boston, 2015.
[35] C. Gu, J. Lian, Y. Bao, et al., Numerical study of the effect of inclusions on the residual stress distribution in high-strength martensitic steels during cooling, Appl. Sci. 9 (2019), https://doi.org/10.3390/app9030455.
[36] A.A. Griffith, The phenomena of rupture and flow in solids, Philos Trans. R Soc. A Math. Phys. Eng. Sci. C (1920) 163–198.
[37] A. Lambert-Perlade, A.F. Gourgues, J. Besson, et al., Mechanisms and modeling of cleavage fracture in simulated heat-affected zone microstructures of a high-strength low alloy steel, Metall. Mater. Trans. A Phys. Metall. Mater. Sci. 35 (2004) 1039–1053, https://doi.org/10.1007/s11661-004-1007-6.
[38] X. Li, X. Ma, S.V. Subramanian, et al., Structure–property–fracture mechanism correlation in heat-affected zone of X100 Ferrite−Bainite pipeline steel, Metall. Mater. Trans. E 2 (2015) 1–11, https://doi.org/10.1007/s40553-014-0036-3.
[39] X.L. Wang, Y.R. Nan, Z.J. Xie, et al., Influence of welding pass on microstructure and toughness in the reheated zone of multi-pass weld metal of 550 MPa offshore engineering steel, Mater. Sci. Eng., A 702 (2017) 196–205, https://doi.org/10.1016/j.msea.2017.06.081.
[40] W.R. Tyson, R.A. Ayres, D.F. Stein, Anisotropy of cleavage in B.C.C. transition metals, Acta Metall. 21 (1973) 621–627, https://doi.org/10.1016/0001-6160(73)90071-0.
[41] C. Berejnoi, J.E. Perez Ipiña, C.L. Llorente, Reproducibility of pop-ins in laboratory testing of welded joints, Mater. Res. 3 (2000) 139–146, https://doi.org/10.1590/s1516-14392000000400008.
[42] H.G. Pisarski, R. Hammond, K. Watt, Significance of splits and pop-ins observed during fracture toughness testing of line pipe steel, in: Proceedings of the IPC 2008, 7th International Pipeline Conference, 2008.
[43] T. Kyada, J.R. Shant, R.K. Goyal, T.S. Kathayat, Understanding the delamination and its effect on charpy impact energy in thick wall linepipe steel, J. Mater. Metall. Eng. 4 (2014) 31–39.
[44] A. Neimitz, J. Galkiewicz, I. Dzioba, The ductile-to-cleavage transition in ferritic Cr-Mo-V steel: a detailed microscopic and numerical analysis, Eng. Fract. Mech. 77 (2010) 2504–2526, https://doi.org/10.1016/j.engfracmech.2010.06.003.
[45] D.C. Ramachandran, S.D. Kim, J. Moon, et al., Classification of martensite-austenite constituents according to its internal morphology in high-strength low alloy steel, Mater. Lett. 278 (2020), https://doi.org/10.1016/j.matlet.2020.128422.